Effects of crystal structure on Co-$L_{2,3}$ x-ray absorption near-edge structure and electron-energy-loss near-edge structure of trivalent cobalt oxides

Yu Kumagai, Hidekazu Ikeno, Fumiyasu Oba, Katsuyuki Matsunaga, and Isao Tanaka

Department of Materials Science and Engineering, Kyoto University, Yoshida, Sakyo, Kyoto 606-8501, Japan

Co-$L_{2,3}$ x-ray-absorption near-edge structures (XANES) and electron-energy-loss near-edge structures (ELNES) are calculated from first principles, taking into account the configuration interactions among molecular orbitals for model clusters obtained using fully-relativistic one-electron calculations. The spectra for $LaCoO_3$ at low temperature and for $LiCoO_2$, both of which have low-spin Co^{3+} ions in similar local environments, are well reproduced. To elucidate the cause of the spectral shape, the effects of the crystal structure and coordination distance are investigated using idealized crystal structures of layered rock salt, perovskite, rock salt, and spinel. The calculated spectra for these crystals with the same coordination distance are found to show clear differences despite identical $3d$ electronic configurations and local environments of the first ligand shell. The crystal structure dependence can be explained by the difference in the Madelung potential acting on the $3d$ orbitals. The results of the calculations for various coordination distances indicate that not only the crystal field splitting parameter, namely, $10Dq$, but also the coordination distance is a key factor in determining the spectral shape. This is attributed to the change in the spatial distribution of the $3d$ orbitals.

I. INTRODUCTION

In $3d$ transition-metal (TM) compounds, $3d$ electrons play a central role in determining their macroscopic properties. X-ray-absorption near-edge structures (XANES) as well as electron-energy-loss near-edge structures (ELNES) at TM-L_2 and -L_3 edges have been widely used to characterize the TM $3d$ electronic states.[1–7] Both of them provide almost identical spectra, which mainly correspond to the electronic dipole excitation of $2p_{1/2}$ and $2p_{3/2}$ core electrons to unoccupied $3d$ bands. Minor contributions, such as those from electronic quadrupole transition and excitation to $4s$ bands, are typically negligible. In general, the main features of TM-$L_{2,3}$ XANES/ELNES are determined from three factors, namely, the oxidation and the spin states of TM $3d$ elements and the coordination number of TM atoms. Other factors, such as ligand species, coordination distance, and crystal structure, are considered to affect the fine shape of the spectrum, but their contributions have not been well established. To acquire quantitative information on the local atomic and electronic structures from TM-$L_{2,3}$ XANES/ELNES, the effects of each individual factor should be understood. Theoretical approaches are suited to this purpose.

In the theoretical studies of TM-$L_{2,3}$ XANES/ELNES, a crystal-field atomic-multiplet method, which aims to reproduce spectra by incorporating crystal field effects into an atomic multiplet calculation,[1–4] is often employed. The effects of the oxidation and spin states of TM $3d$ elements, the coordination number of TM atoms and ligand species on TM-$L_{2,3}$ XANES/ELNES were investigated by the crystal-field atomic-multiplet method.[3] However, the contributions of the crystal structure and coordination distance have not been discussed quantitatively. An important effect of the crystal structure for ionic crystals is the electrostatic potential generated by constituent ions, namely, the Madelung potential (MP). When the array of ions surrounding a TM atom is different between crystals such as perovskite and layered

rock salt, the Madelung potential around the TM atom should be different. Then, both covalency between the TM and ligand and crystal field splitting, often represented by $10Dq$, change because of the change in the $3d$ orbitals spatial distribution. The coordination distance should also affect these properties. The crystal-field atomic-multiplet method implicitly reflects these effects via two or more parameters, such as crystal field splitting and reduced Slater-Condon parameters. In contrast, first principles approaches are straightforward since crystal structure and coordination distance are directly considered as input structures.

A first principles method has been developed by the present authors to calculate the multiplet structures. This method has been successful in reproducing the experimental spectra and providing proper interpretation of their multiplet structures.[8–11] It has been established that experimental XANES and ELNES at simple element K edges can be well reproduced by first principles calculations within the framework of the one-electron theory if the core-hole effect is properly taken into account.[12] On the other hand, the one-electron theory generally fails to explain the spectral shape of TM-$L_{2,3}$ XANES/ELNES because the spatial localization of the TM $3d$ electrons and core $2p$ electrons brings about a strong correlation among them. In our approach, the electronic correlation relevant to TM-$L_{2,3}$ XANES/ELNES is taken into account via the configuration interaction (CI) among fully relativistic molecular orbitals (MO). TM-$L_{2,3}$ XANES/ELNES are obtained as matrix elements of electronic dipole transition using the calculated many-electron wave functions. The effects of the Madelung potential are taken into account by embedding the cluster into an array of point charges.

In the present study, we examine trivalent cobalt oxide compounds. Cobalt oxides are important in modern technology as a cathode material of the lithium ion battery ($LiCoO_2$) (Ref. 13) and thermo electrics (Na_xCoO_2) (Ref. 14) to mention a few examples. A spin-crossover transition of $LaCoO_3$

with temperature has been the subject of fundamental studies since the late 1950s.[15–19] Many experimental reports of Co-$L_{2,3}$ XANES are available in the literature for a few cobaltites including LaCoO$_3$ and LiCoO$_2$.[20–24] There are clear differences between the spectra of LaCoO$_3$ and LiCoO$_2$. It is interesting that the spectral shape is dependent on the crystal structure even when the oxidation and spin states, and the local environment of the first ligand shell (i.e., coordination number and coordination distance) are similar. First, we examine the effects of the Madelung potential on the spectral shape using the models for four crystals, i.e., layered rock salt, perovskite, rock salt, and spinel. The relative height and relative energy of the subpeak to the main peak are used to characterize the spectral shape. Second, the effects of the Co-O bond length are examined using theoretical spectra of CoO$_6^{9-}$ clusters with different Co-O bond lengths.

II. COMPUTATIONAL PROCEDURES

All the calculations were carried out using the model cluster CoO$_6^{9-}$. The effects of the Madelung potential were included by embedding the cluster into the array of point charges. An artificial electronic dipole generated by the point charges was eliminated by manipulating the charge at the outermost points by the Evjen method.[25] The total number of electrons in the cluster was 84. The exchange-correlation (XC) interactions among Co $2p$, $3d$, and six-coordinated O $2p$ electrons (total of 48 electrons) were considered directly by the configuration interaction (CI) method, which we called the TM $2p$TM $3d$+O $2p$-multiplet approach in Ref. 10. The other electrons (Co $1s$, $2s$, $3s$, $3p$, O $1s$, $2s$) were considered to be less important for the Co-$L_{2,3}$ XANES/ELNES because they do not strongly interact with Co $2p$, $3d$ electrons. Regarding these electrons, the XC interactions were incorporated by adopting the Dirac-Fock-Slater approximation.[8] The spin-orbit coupling of Co $2p$ electrons is included by solving the Dirac equation. The relativistic many-electron Hamiltonian is expressed as

$$H = \sum_{i=1}^{N} h(\boldsymbol{r}_i) + \sum_{i=1}^{N}\sum_{j<i} \frac{1}{|\boldsymbol{r}_i - \boldsymbol{r}_j|}, \quad (1)$$

where

$$h(\boldsymbol{r}_i) = c\tilde{\boldsymbol{\alpha}} \cdot \boldsymbol{p}_i + c^2\tilde{\beta} - \sum_{\nu=1}^{P} \frac{Z_\nu}{|\boldsymbol{r}_i - \boldsymbol{R}_\nu|} + V^{\mathrm{MP}}(\boldsymbol{r}_i) + V'(\boldsymbol{r}_i). \quad (2)$$

Atomic units are used throughout this article. $\tilde{\boldsymbol{\alpha}}$ and $\tilde{\beta}$ are the Dirac matrices represented by 4×4 matrices. c is the light

velocity. $\boldsymbol{p}_i$ is the momentum operator of the ith electron. $\boldsymbol{r}_i$ and $\boldsymbol{R}_\nu$ are the positions of the ith electron and the νth nucleus, respectively. Z_ν is the charge of the νth nucleus. N in Eq. (1) is the number of electrons considered in the CI calculations. P in Eq. (2) is the number of nuclei in the model cluster. In the present case, $N=48$ and $P=7$. $V^{\mathrm{MP}}(\boldsymbol{r})$ is the Madelung potential applied by the external ions to the cluster and is given by

$$V^{\mathrm{MP}}(\boldsymbol{r}) = \sum_i \frac{q_i}{|\boldsymbol{r} - \boldsymbol{R}_i|} - \sum_{\nu=1}^{P} \frac{q_\nu}{|\boldsymbol{r} - \boldsymbol{R}_\nu|}, \quad (3)$$

where q_i is the charge of ions. The second term on the right-hand side of Eq. (3) corresponds to the contribution from the ions in the model cluster and is subtracted from the first term which gives the summation over all the ion sites. $V'(\boldsymbol{r}_i)$ in Eq. (2) is the Coulomb and XC potential for 36 electrons that are not taken into account in the CI calculations. The explicit form of $V'(\boldsymbol{r}_i)$ was derived by Watanabe and Kamimura.[26]

First, we obtained four-component fully-relativistic one-electron molecular orbitals using numerical atomic orbitals as basis functions.[27] The XC interactions were considered by adopting the Dirac-Fock-Slater approximation. The obtained one-electron molecular orbitals were then used as the basis functions of many-electron CI calculations. Many-electron wave functions are expressed as a linear combination of the Slater determinants,

$$\Psi = \sum_{p=1}^{M} C_p \Phi_p, \quad (4)$$

where M is the number of the Slater determinants. Φ_p and C_p are the pth Slater determinants expressed as an electronic configuration and its coefficient, respectively. To reduce the computational effort, we took into account only the one-electron excitation process from the Co $2p$ core level to the Co $3d$ unoccupied states. The charge transfer of O $2p$ electrons to Co $3d$ unoccupied states was not considered.

We considered the low-spin state (LS) to be the ground state of Co^{3+}; it is an experimentally reported spin state in LaCoO$_3$ under low temperature and LiCoO$_2$. In the LS state, the six t_{2g} orbitals are fully occupied and the four e_g orbitals are not occupied at all. Therefore, the initial electronic configuration is (Co $2p$)^6(O $2p$)^{36}(t_{2g})^6(e_g)^0 and the corresponding number of the Slater determinant is $_6C_6 \times _{36}C_{36} \times _6C_6 \times _4C_0 = 1$. In the excited states, $3d$ electrons can take all possible configurations. The final electronic configurations are denoted as (Co $2p$)^5(O $2p$)^{36}($t_{2g}e_g$)^7 and the corresponding number of Slater determinants is $_6C_5 \times _{36}C_{36} \times _{10}C_7 = 720$.

TABLE I. Experimental crystal structures of LaCoO$_3$ and LiCoO$_2$.

	Crystal structure	Space group	Site symmetry on Co^{3+} ions	Co-O bond length (Å)	O-Co-O bond angle
LaCoO$_3$ [a]	Perovskite	$R\bar{3}c$ (167)	C_{3i}	1.925	88.5°
LiCoO$_2$ [b]	Layered rock salt	$R\bar{3}m$ (166)	D_{3d}	1.921	85.8°

[a]Reference 28.
[b]Reference 29.
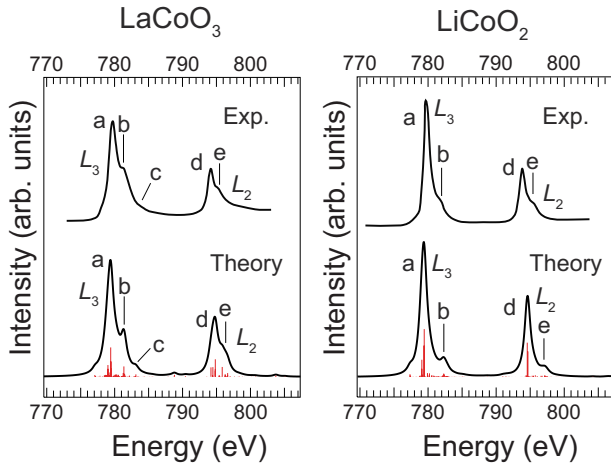
FIG. 1. (Color online) Theoretical Co L$_{2,3}$-edge XANES for LaCoO$_3$ and LiCoO$_2$ compared with experimental spectra. The initial spin state of calculated spectra is fixed to low-spin state. The experimental spectra are taken from Refs. [20] and [21].

Thus, 721 Slater determinants were considered in total. By diagonalizing the Hamiltonian in Eq. (1), we obtained the many-electron eigenvalues and eigenvectors, which correspond to many-electron energies and wave functions, respectively, relevant to the Co-L$_{2,3}$ XANES/ELNES.

The oscillator strengths of electronic dipole transition were calculated using many-electron wave functions. Theoretical spectra were obtained by broadening the oscillator strengths using a Lorentzian function of FWHM=1.0 eV.

III. RESULTS AND DISCUSSION

A. Theoretical Co-L$_{2,3}$ XANES of LaCoO$_3$ and LiCoO$_2$

Figure 1 shows theoretical Co-L$_{2,3}$ XANES of LaCoO$_3$ and LiCoO$_2$, together with experimental spectra.[20,21] Both their ground states are known to be the LS state.[16–21] LaCoO$_3$ exhibits LS only at low temperatures. Thus, the experimental spectrum of the low-temperature phase of LaCoO$_3$ is shown in Fig. 1. The theoretical spectra were obtained using the CoO$_6^{9-}$ cluster based on the experimental crystal structures[28,29] (Table I). The present CI calculations overestimate the absolute absorption energy because they do not include all the electronic correlation, as mentioned above. Our previous study has shown that the absorption energy is well estimated by Slater's transition-state method.[8] The absorption onset of the spectra shown in Fig. 1 was determined using the same approach. The theoretical spectra are in good agreement with the experimental spectra for both crystals. Some subpeaks can be recognized in both L$_3$ and L$_2$ spectra. The intensities of subpeaks b and e in LiCoO$_2$ are lower than those in LaCoO$_3$. Subpeak c, which exists in the LaCoO$_3$ spectrum, is not clearly recognized in the LiCoO$_2$ spectrum. The relative height of subpeak b to main peak a, I_b/I_a, and the relative energy of subpeak b to main peak a, E_b-E_a, are hereafter used to characterize the spectral shape.

In order to further investigate the effects of crystal structure on the spectral shape, a set of calculations is carried out using the same CoO$_6^{9-}$ cluster embedded in different external potentials corresponding to idealized LaCoO$_3$ (perovskite; PE) and LiCoO$_2$ (layered rock salt; LRS) crystals, as shown in Table II. The cluster has a regular octahedral symmetry (O$_h$) with the Co-O bond length R of 1.92 Å. Because of the presence of the external potential, the site symmetry of Co^{3+} ions in the LRS crystal is reduced to D_{3d}, whereas that of PE remains O$_h$. The theoretical spectra for the ideal perovskite and layered rock salt structures are displayed in Fig. 2. The spectra are almost the same as those shown in Fig. 1, which were computed with clusters based on real crystals (Table I). This fact means that a slight distortion of the crystal or change in the coordination distance does not affect the spectra.

In Fig. 2, the composition of final configurations for many-electron eigenstates is also shown. Here, the TM 3d orbitals are expressed using Mulliken notations under O$_h$ symmetry, t_{2g} and e_g, for simplicity, although the present calculations are based on relativistic quantum mechanics and the point symmetry at the Co^{3+} site is lowered from O$_h$ in some of the crystals considered. The many-electron states are decomposed into the final one-electron configurations, for example, $(2p)^5(t_{2g})^6(e_g)^1$ and $(2p)^5(t_{2g})^5(e_g)^2$. The composi-

TABLE II. Space group, lattice constants, atomic positions, and site symmetry on Co^{3+} ions for ideal crystal structures. Co^{3+} ions are located at the B site in the layered rock salt, perovskite, and spinel.

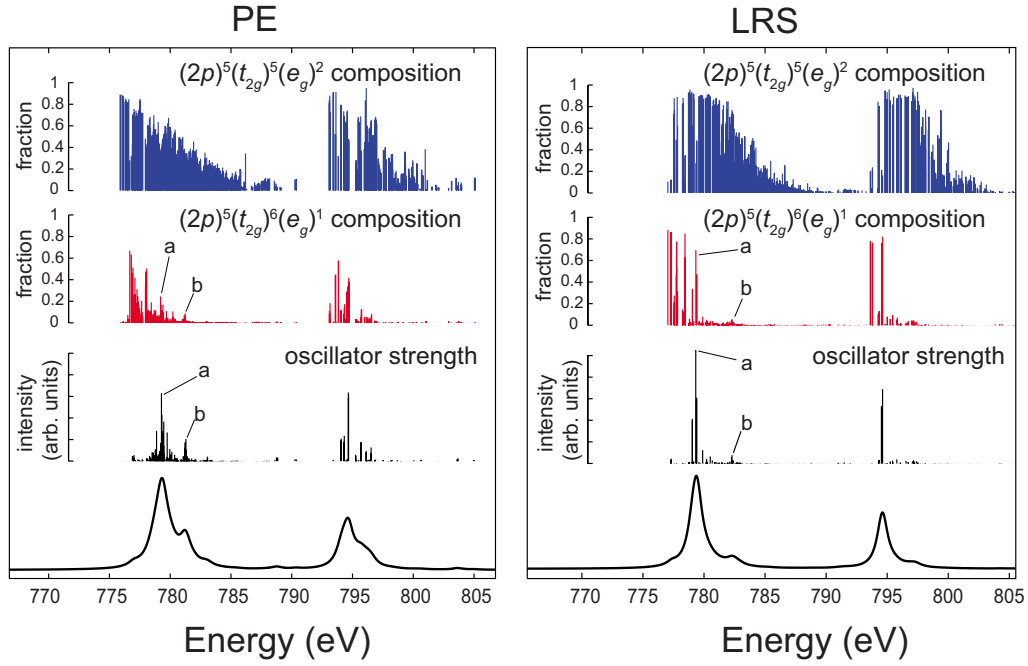|	Space group	Lattice constants Å	Atomic positions	Site symmetry on Co^{3+} ions
Layered rock salt (ABO_2)	$R\bar{3}m$ (166)	$a=b=2.734$ $c=13.441$	A$^+$ (0.333,0.667,0.167) B^{3+} (0,0,0) O^{2-} (0.667,0.333,0.083)	D_{3d}
Perovskite (ABO_3)	$Pm\bar{3}m$ (221)	$a=3.380$	A^{3+} (0.5,0.5,0.5) B^{3+} (0, 0, 0) O^{2-} (0.5,0.5,0)	O$_h$
Rocksalt (AO)	$Fm\bar{3}m$ (225)	$a=3.380$	A^{2+} (0.5,0.5,0.5) O^{2-} (0,0,0)	O$_h$
Spinel (AB_2O_4)	$Fd\bar{3}m$ (227)	$a=7.760$	A^{2+} (0,0,0) B^{3+} (0.625,0.625,0.625) O^{2-} (0.375, 0.375, 0.375)	D_{3d}

FIG. 2. (Color online) (Bottom) Theoretical Co-$L_{2,3}$ XANES for Co^{3+} with low-spin state in idealized perovskite (PE) and idealized layered rock salt (LRS). (Second bottom) The corresponding oscillator strength for multielectron eigenstates. (Top and second top) The composition of final configurations for $(2p)^5(t_{2g})^6(e_g)^1$ and $(2p)^5(t_{2g})^5(e_g)^2$.

tions of $(2p)^5(t_{2g})^6(e_g)^1$ and $(2p)^5(t_{2g})^5(e_g)^2$ for each final state are shown in Fig. 2. The intensity of the oscillator strength is also shown. This type of diagram was given in our previous report.[10,11] Two points should be kept in mind. One is that the final configurations, except for $(2p)^5(t_{2g})^6(e_g)^1$, are not allowed by the electronic dipole transition from the initial configuration of $(2p)^6(t_{2g})^6(e_g)^0$. Second, the final configuration of $(2p)^5(t_{2g})^6(e_g)^1$ does not equally contribute to the oscillator strength at each state because the dipole transition matrix elements vary depending upon the spatial distribution of many-electron wave functions. As can be seen in Fig. 2, the composition of $(2p)^5(t_{2g})^6(e_g)^1$ is 69.4% for peak a of LRS, whereas it is only 5.6% for peak b of LRS. In other words, the many-electron eigenstate at peak a mainly comprises the $(2p)^5(t_{2g})^6(e_g)^1$ configuration, whereas that at peak b comprises the $(2p)^5(t_{2g})^5(e_g)^2$ or higher excitation configurations. The energy difference between the final configurations of $(2p)^5(t_{2g})^6(e_g)^1$ and $(2p)^5(t_{2g})^5(e_g)^2$ could be related to the one-electron energy difference between the t_{2g} and e_g orbitals, i.e., the crystal field splitting value, $10Dq$, at the ground state. With smaller $10Dq$, we expect decreasing $E_b - E_a$, and hence the configurations of $(2p)^5(t_{2g})^6(e_g)^1$ and $(2p)^5(t_{2g})^5(e_g)^2$ mix well, which would increase the I_b/I_a ratio. The $10Dq$ of Co^{3+} in PE and LRS are estimated to be 1.80 and 2.25 eV, respectively, using the averaged relativistic one-electron energies corresponding to the e_g and t_{2g} orbitals. As a matter of fact, $E_b - E_a$ of PE, in which $10Dq$ of Co^{3+} is 0.45 eV smaller than that in LRS, is smaller and I_b/I_a is larger than those of LRS, as can be seen in Fig. 2.

B. Crystal structures and external potentials

The effects of the Madelung potential on the spectral shape are further examined for two more crystals, i.e., rock

salt (RS) and spinel (SP) (Table II). In the present SP crystal, the normal spinel arrangement of trivalent cations at the octahedral site is assumed. For RS in which the constituent cations are divalent, we assume that trivalent Co impurity is dissolved into the RS host crystal. Calculations were made using the same CoO_6^{9-} cluster as that used in the case of Fig. 2. The site symmetry of Co^{3+} ions in RS is O_h, whereas it is D_{3d} in SP (Table II).

In Fig. 3, the relative value of $V^{MP}(r)$ to the value at the Co^{3+} site located at the center of the cluster, $\Delta V^{MP}(r)$, is shown. The CoO_6^{9-} clusters are superposed on the figure. The white zone of the potential maps indicates the space with $\Delta V^{MP} \approx 0$. It is interesting that the shape and the area of $\Delta V^{MP}(r)$ are clearly dependent on the crystal structure. The white zone appears to be the largest in PE and the second largest in RS.

The results presented in Fig. 1 demonstrate that the use of formal charges for the Madelung potential well reproduces the experimental spectra of the Co compounds. We applied the same approach to a variety of systems and found an agreement with experimental spectra at a similar level.[8–11] Therefore, there is no need to vary the charges for Madelung potential. However, it is important to investigate the effects of the strength of the Madelung potential. In order to trace the transitions of spectra through the change in the strength of the Madelung potential, we applied an artificial Madelung potential, $V^{MP,Q}(r)$, given as

$$V^{MP,Q}(\mathbf{r}) = Q \cdot V^{MP}(\mathbf{r}), \tag{5}$$

where Q is a reduction/enhancement factor. The reduction limit, $Q=0$, corresponds to the isolated model without the Madelung potential.
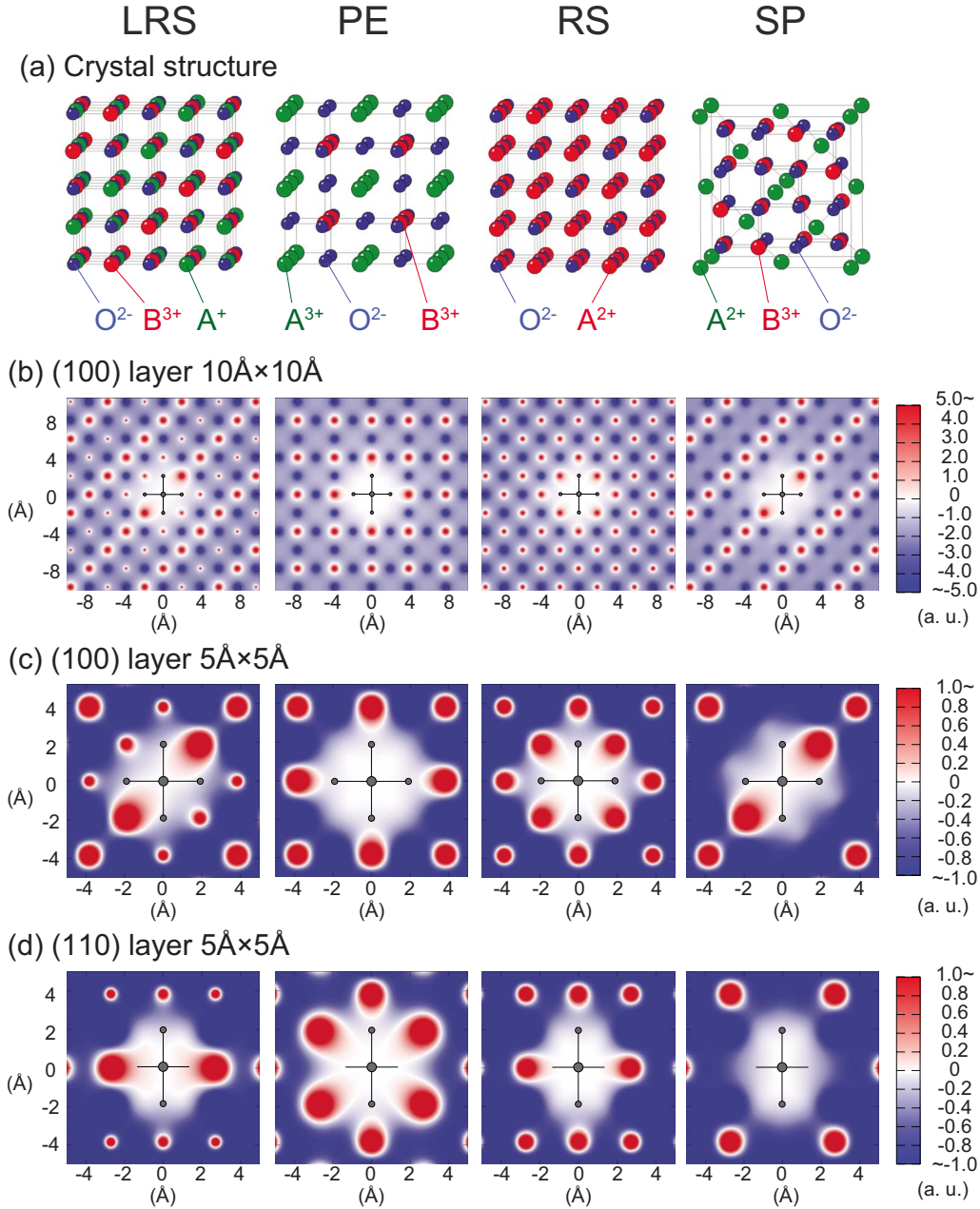
FIG. 3. (Color online) (a) Crystal structures of layered rock salt (LRS), perovskite (PE), rock salt (RS), and spinel (SP). [(b), (c)] Madelung potential around the CoO_6^{9-} cluster for each structure on the (100) plane. (d) The same potential on the (110) plane.

A rigid shift of the Madelung potential for all the $3d$ orbitals does not affect the relative peak positions, whereas the difference between the potentials for respective orbitals should be important in determining the spectral shape. We define the difference between the Madelung potential for the t_{2g} and e_g orbitals as

$$\Delta E^{MP} = \langle e_g | V^{MP,Q} | e_g \rangle - \langle t_{2g} | V^{MP,Q} | t_{2g} \rangle, \quad (6)$$

where the averaged Madelung potential that acts on each orbital is specified by $\langle e_g | V^{MP,Q} | e_g \rangle$ and $\langle t_{2g} | V^{MP,Q} | t_{2g} \rangle$. Figure 4 shows ΔE^{MP} as a function of Q. As expected from the maps of $\Delta V^{MP}(\boldsymbol{r})$ in Fig. 3, ΔE^{MP} of PE, which has the largest white zone of $\Delta V^{MP}(\boldsymbol{r})$, is almost insensitive to Q. In the

other three crystals, ΔE^{MP} increases almost proportionally to Q.

Since V^{MP} is part of the one-electron Hamiltonian, ΔE^{MP} should be related to $10Dq$ calculated using one-electron energies. Figure 5 shows the relationship between ΔE^{MP} and $10Dq$ for the four crystals with different Q values. The value of $10Dq$ for an isolated cluster model is also shown at $\Delta E^{MP}=0$. With the increase in ΔE^{MP}, $10Dq$ increases. All the $10Dq$ values of different crystal structures are located nearly on the same line with the gradient of 0.46, which means that the V^{MP} term in the one-electron Hamiltonian directly contributes to the increment of $10Dq$ by only 46%. The other terms in the one-electron Hamiltonian reduce $10Dq$ significantly through the screening of the Madelung potential
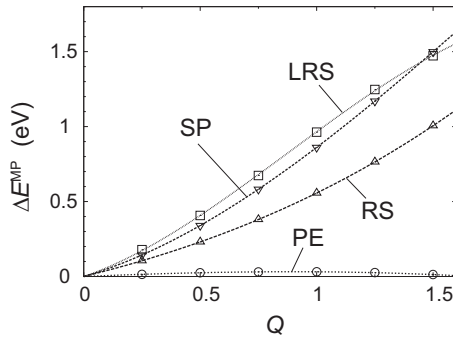
FIG. 4. Difference between the Madelung potential acting on e_g and t_{2g} orbitals as a function of the reduction/enhancement factor, Q. $Q=1$ corresponds to the potential generated using formal charges.
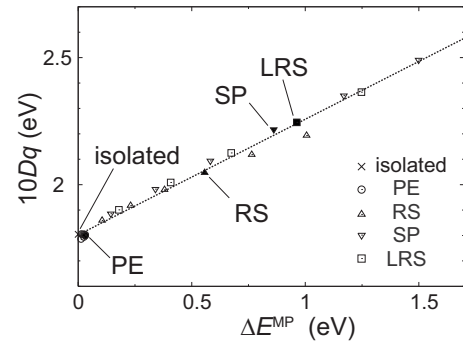

FIG. 5. Relationship between the difference between the Madelung potential acting on e_g and t_{2g} orbitals and the magnitude of $10Dq$ at the ground state. The Co-O bond length in the CoO_6^{9-} cluster is fixed at 1.92 Å. The reduction/enhancement factor of the Madelung potential, Q, is set at 0, 0.25, 0.5, 0.75, 1, 1.25, and 1.5. Filled marks denote the values with $Q=1$.

and/or the relaxation of $3d$ orbitals. A detailed discussion on the spatial distribution of the e_g orbitals is given later at Sec. III D.

C. Effects of Madelung potential on spectral shape

Figure 6 shows a series of theoretical Co-$L_{2,3}$ XANES of the four crystals obtained for the ideal octahedral CoO_6^{9-} clusters with varying Q. As can be seen, the spectral shape, as represented by I_b/I_a and E_b-E_a, does not change markedly in PE. On the other hand, in the other crystals, I_b/I_a decreases with the increase in Q and eventually, peak b vanishes with large Q. The same behavior can be observed for peaks d and e.

In order to clarify the relationships between the strength of the Madelung potential and the spectral shape, the depen-

dences of E_b-E_a and I_b/I_a on ΔE^{MP} were investigated. The results are summarized in Fig. 7. As recognized, both E_b-E_a and I_b/I_a are simply determined by ΔE^{MP} independently of crystal structures. E_b-E_a and I_b/I_a for the PE crystal, showing a nearly zero ΔE^{MP} irrespective of the Q value (see Fig. 4), are close to those of the isolated cluster. On the other hand, E_b-E_a and I_b/I_a of SP and LRS with similar trends of ΔE^{MP} are similar to each other. Thus, the Madelung potential acting on respective orbitals is an essential factor in determining the spectral shape.

D. Effects of Co-O bond length on spectral shape

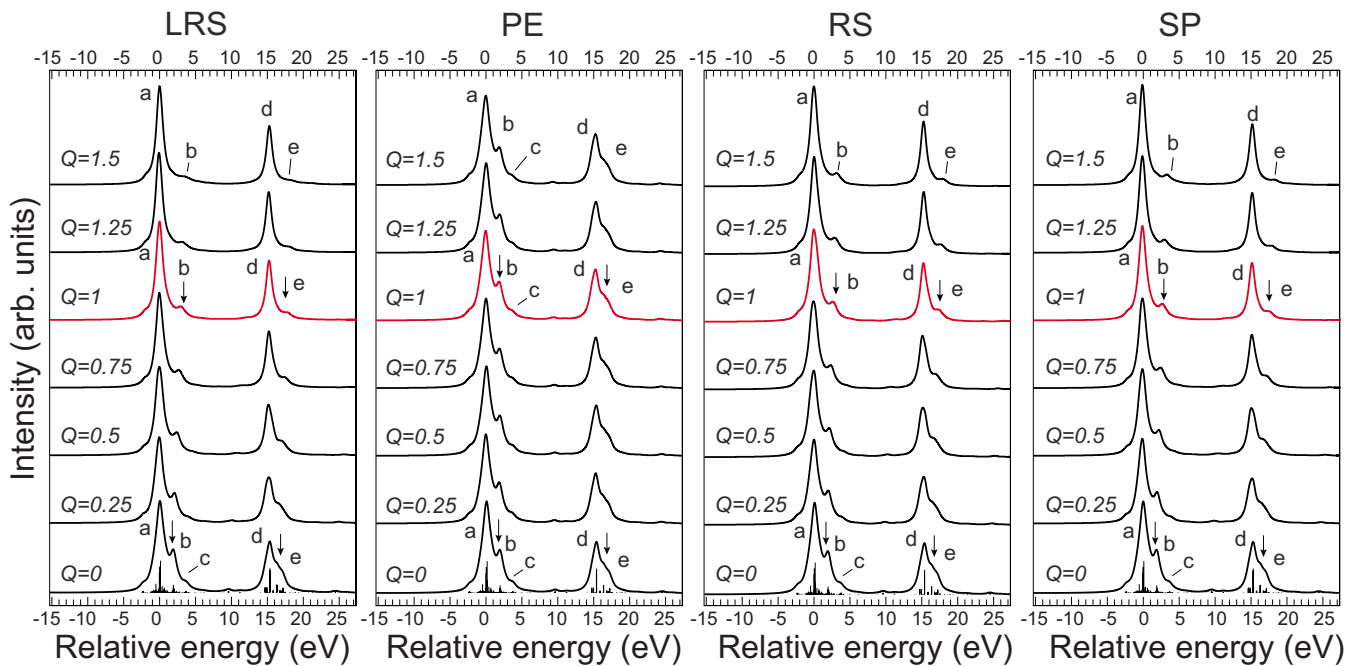The results presented in Figs. 2–7 were obtained using model clusters with the Co-O bond length, R, fixed at

FIG. 6. (Color online) Theoretical Co-$L_{2,3}$ XANES with low-spin initial spin state with varying the reduction/enhancement factor of the Madelung potential, Q. Q is set at 0, 0.25, 0.5, 0.75, 1, 1.25, and 1.5. The third spectrum from the top (highlighted by red) corresponds to the case with $Q=1$.
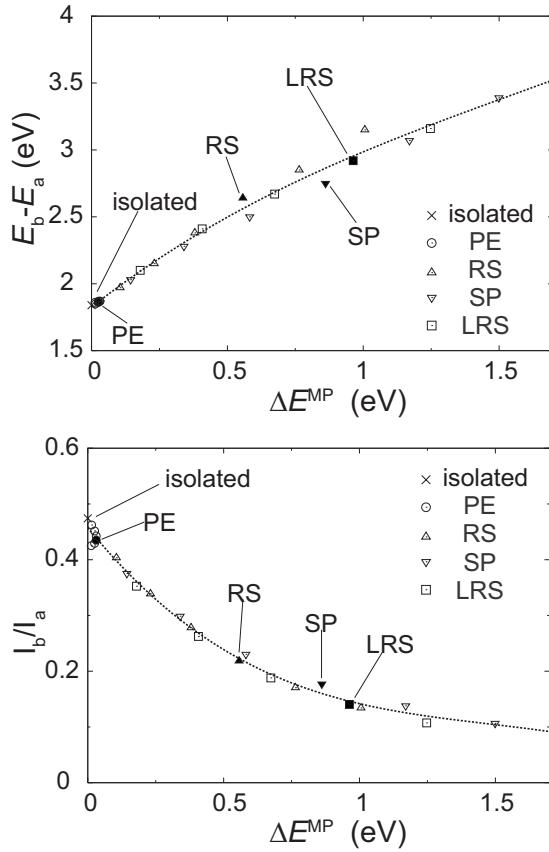
FIG. 7. Energy and height of subpeak b relative to those of main-peak a as a function of ΔE^{MP}. The Co-O bond length in the CoO$_6^{9-}$ cluster was fixed at 1.92 Å. Values with $Q=0$, 0.25, 0.5, 0.75, 1, 1.25, and 1.5 are included. Filled marks denote the values with $Q=1$.

1.92 Å. Two additional sets of calculations are carried out for the four crystals and the isolated cluster with $R=1.82$ and 2.02 Å. Their I_b/I_a vs $10Dq$ relationships are shown with that of $R=1.92$ Å in Fig. 8. It is very interesting that I_b/I_a values obtained for different R are located on different curves. This finding means that the spectral shape is dependent not only on $10Dq$ but also on R or another alternative quantity. For example, when $10Dq$ is 1.8 eV, I_b/I_a differs from 0.20 to 0.47 depending upon R in the range of 1.92–2.02 Å.

As an example of the R-dependence, theoretical spectra for isolated clusters in O$_h$ symmetry are shown in Fig. 9. The values of $10Dq$ are also shown. Their I_b/I_a values are located on the broken line in Fig. 8. As can be seen in Fig. 9, the change in I_b/I_a with the change in $R \pm 0.1$ Å is much smaller than the effects of the Madelung potential in the different crystals with fixed R. The key to explaining the results resides in the spatial distribution of the e_g orbitals. As represented in the computational procedures section, the $2p$ core electrons of Co^{3+} ions are excited to the e_g orbitals, which are not occupied at all. Since the Madelung potential depends on the crystal structure, as shown in Fig. 3, the spatial distribution of the e_g orbitals is different for each crystal structure. To illustrate this difference, the charge distribution of the e_g orbitals in LRS and PE is examined here.
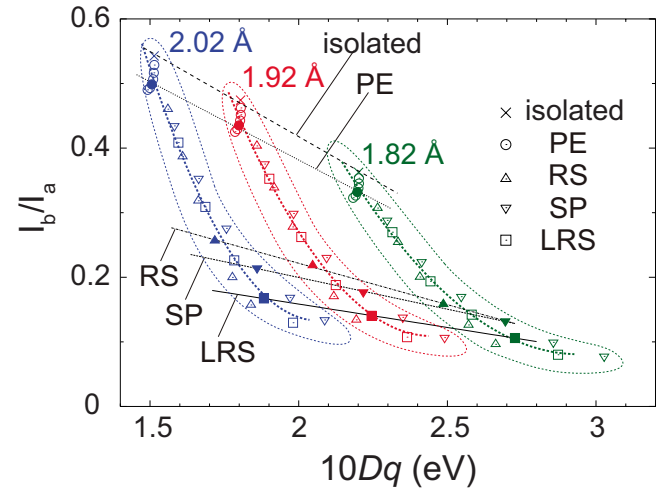

FIG. 8. (Color online) Relative intensity between peaks b and a as a function of $10Dq$. Values with the Co-O bond length $R=1.82$, 1.92, and 2.02 Å, and $Q=0$, 0.25, 0.5, 0.75, 1, 1.25, and 1.5 are included. Filled marks denote the values with $Q=1$. The straight lines (solid, dashed, or dotted) connect the results with $Q=1$. The dotted curves enclose the results with the same R.

The averaged charge density of the four e_g orbitals is obtained by

$$\rho_{e_g}(\boldsymbol{r}) = \frac{1}{4}\sum_{i=1}^{4}|\varphi_{e_g}^{(i)}(\boldsymbol{r})|^2. \tag{7}$$

R for the two models is fixed at 1.92 Å. The difference in the spatial distribution, $\Delta\rho_{e_g}(\boldsymbol{r}) = \rho_{e_g}^{LRS} - \rho_{e_g}^{PE}$, on the (100) plane is shown in Fig. 10(a). As can be seen in the map, $\rho_{e_g}^{LRS}(\boldsymbol{r})$ and $\rho_{e_g}^{PE}(\boldsymbol{r})$ are somewhat different, which can be explained by the difference in the Madelung potential for the e_g orbitals. The charge density is distributed more toward the trivalent cation site in LRS than in PE. Except for this direction, the charge density in LRS is lower in the vicinity of the Co^{3+} site. Another noteworthy characteristic is the higher charge density at the O^{2-} site in LRS. This indicates a greater contribution of the O-$2p$ orbitals to the e_g orbitals, i.e., a stronger covalency.

In order to evaluate the spatial distribution of the e_g orbitals, the average radius is calculated as

$$\langle r \rangle_{e_g} = \frac{1}{4}\sum_{i=1}^{4}\langle\varphi_{e_g}^{(i)}|r|\varphi_{e_g}^{(i)}\rangle. \tag{8}$$

Figure 10(b) shows the relationship between $10Dq$ and $\langle r \rangle_{e_g}$ for the four crystals and the isolated cluster with different Q and R. In the case of the isolated cluster ($Q=0$), $\langle r \rangle_{e_g}$ decreases with the decrease in R, as designated by the broken line in Fig. 10. $10Dq$ increases with the decrease in R. These tendencies are for the simple geometric effects, and lead to the increase of $10Dq$ with the decrease in $\langle r \rangle_{e_g}$. The same trend is recognized for the four crystal structures with $Q=1$, as indicated by the other lines. On the other hand, $10Dq$ increases with the increase in $\langle r \rangle_{e_g}$ when Q, i.e, ΔE^{MP}, is varied with a fixed R (the corresponding series of data are

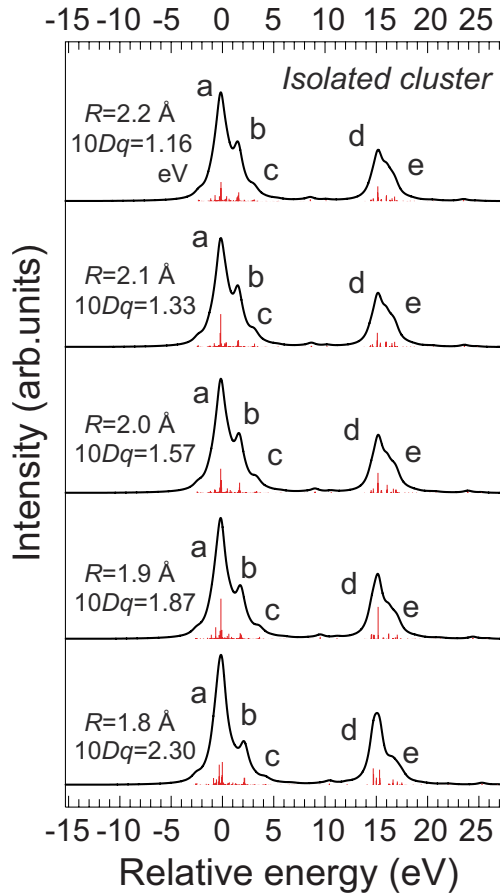FIG. 9. (Color online) Theoretical Co-$L_{2,3}$ XANES for isolated clusters in O$_h$ symmetry with varying Co-O bond lengths, R.
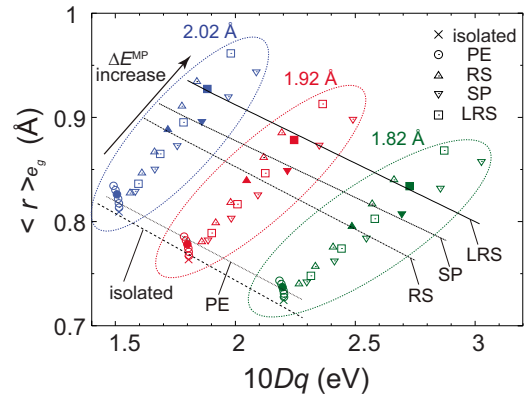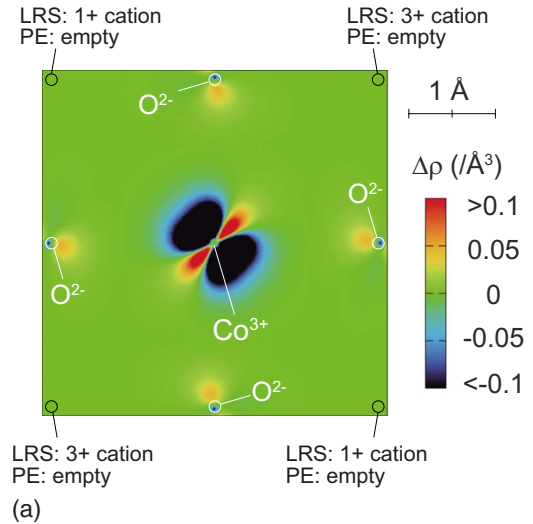

FIG. 10. (Color online) (a) Difference in partial charge distributions of the e_g orbitals between PE and LRS with $R = 1.92$ Å, $\Delta\rho = \rho_{LRS} - \rho_{PE}$. (b) Averaged radial distance of e_g orbitals, $\langle r \rangle_{e_g}$, calculated for different Madelung potential and R, as a function of $10Dq$. Q is set at 0, 0.25, 0.5, 0.75, 1, 1.25, and 1.5. Filled marks denote the values with $Q = 1$. The straight lines connect the results with $Q = 1$ and the dotted curves enclose the results with the same R.

enclosed by dotted curves). This is a result of the effects of the Madelung potential on respective $3d$ orbitals, as described above. The dependence of $10Dq$ on $\langle r \rangle_{e_g}$ is the opposite in the cases of Q and R. This means that even if $10Dq$ is the same, the spatial distribution of the e_g orbitals could be clearly different. This is the reason why I_b/I_a is not simply governed by $10Dq$ when R is varied.

In the crystal-field atomic-multiplet calculations, two sets of parameters are used to reproduce the TM-$L_{2,3}$ XANES/ ELNES spectra. One is the crystal field parameter, which is $10Dq$ under O$_h$ symmetry. The other is called the reduced Slater-Condon parameter that determines *effective* interactions among $2p$-$3d$ and $3d$-$3d$ electrons in crystals. The strength of covalent bonding and other chemical effects is thought to affect the reduced fraction. The present results demonstrate that the Madelung potential for each $3d$ orbital plays an important role in determining the spectral shape, and it is clearly dependent on the crystal structure. In the crystal-field atomic-multiplet calculations the Slater-Condon parameters should, therefore, be varied in accordance with the crystal structure, even when Co ions have the same oxidation and spin states and the same local environment of the first ligand shell.

IV. CONCLUSION

Theoretical Co-$L_{2,3}$ XANES were obtained for LaCoO$_3$ at low temperature and for LiCoO$_2$ using first principles many-

electron calculations for model clusters that were embedded into the Madelung potential. Isolated clusters with different coordination distances were used for comparison. The major results can be summarized as follows.

(1) Experimental Co-$L_{2,3}$ XANES for the two crystals are reproduced by the calculations using the TM $2p$TM $3d$ +O $2p$-multiplet approach for CoO$_6^{9-}$ clusters on the basis of the experimental crystal structure (Fig. 1). The many-electron final configurations are decomposed into the final one-electron configurations of $(2p)^5(t_{2g})^6(e_g)^1$ and $(2p)^5(t_{2g})^5(e_g)^2$ (Fig. 2). The many-electron eigenstates at peak a mainly originate from the final configurations of $(2p)^5(t_{2g})^6(e_g)^1$, whereas those at peak b correspond to $(2p)^5(t_{2g})^5(e_g)^2$ or higher excitation configurations.

(2) The spatial distribution of the Madelung potential, $V^{MP}(\mathbf{r})$, was examined for four crystals, i.e., PE, RS, SP, and LRS. The shape and the area of the white zone in Fig. 3 ($\Delta V^{MP} \approx 0$) are clearly dependent on the crystal structure.

The white zone is the largest in PE and second largest in RS. The strength of the Madelung potential for the Co-$3d$ orbitals is evaluated by adopting a quantity, ΔE^{MP}, as defined by Eq. (5). As expected from the map, ΔE^{MP} of PE, which has the largest white zone of $\Delta V^{MP}(r)$, is almost insensitive to the different fractions of the Madelung potential, Q (Fig. 4). ΔE^{MP} shows a linear correlation with $10Dq$ (Fig. 5).

(3) The relative height of subpeak b to main peak a, I_b/I_a, and the relative energy of subpeak b to main peak a, $E_b - E_a$, were used to characterize the spectral shape. They do not change markedly with Q in PE, contrary to those in LRS, RS, and SP (Fig. 6). In addition, they are simply determined by ΔE^{MP} independently of the crystal structures when coordination distance, R, is fixed (Fig. 7).

(4) When R is fixed, I_b/I_a is closely related to $10Dq$ in the ground state (Fig. 8). However, I_b/I_a is dependent not only on $10Dq$ but also on R (Fig. 8). This can be explained by considering the spatial distribution of the average radius of the e_g orbitals, i.e., $\langle r \rangle_{e_g}$ (Fig. 10). The correlation between ΔE^{MP} and $10Dq$ is opposite that between R and $10Dq$ (Fig. 10). These results indicate that different reduction parameters are required for different crystal structures in order to analyze the experimental spectra by the crystal-field atomic-multiplet technique.

[1] F. M. F. de Groot, Coord. Chem. Rev. **249**, 31 (2005).

[2] F. M. F. de Groot, Chem. Rev. (Washington, D.C.) **101**, 1779 (2001).

[3] F. M. F. de Groot, J. Electron Spectrosc. Relat. Phenom. **67**, 529 (1994).

[4] F. M. F. de Groot, J. C. Fuggle, B. T. Thole, and G. A. Sawatzky, Phys. Rev. B **42**, 5459 (1990).

[5] W. G. Waddington, P. Rez, I. P. Grant, and C. J. Humphreys, Phys. Rev. B **34**, 1467 (1986).

[6] H. Kurata and C. Colliex, Phys. Rev. B **48**, 2102 (1993).

[7] B. Gilbert, B. H. Frazer, A. Belz, P. G. Conrad, K. H. Nealson, D. Haskel, J. C. Lang, G. Srajer, and G. De Stasio, J. Phys. Chem. A **107**, 2839 (2003).

[8] K. Ogasawara, T. Iwata, Y. Koyama, T. Ishii, I. Tanaka, and H. Adachi, Phys. Rev. B **64**, 115413 (2001).

[9] H. Ikeno, I. Tanaka, T. Miyamae, T. Mishima, H. Adachi, and K. Ogasawara, Mater. Trans. **45**, 1414 (2004).

[10] H. Ikeno, T. Mizoguchi, Y. Koyama, Y. Kumagai, and I. Tanaka, Ultramicroscopy **106**, 970 (2006).

[11] H. Ikeno, I. Tanaka, Y. Koyama, T. Mizoguchi, and K. Ogasawara, Phys. Rev. B **72**, 075123 (2005).

[12] I. Tanaka, T. Mizoguchi, and T. Yamamoto, J. Am. Ceram. Soc. **88**, 2013 (2005).

[13] R. Alcántara, P. Lavela, J. L. Tirado, E. Zhecheva, and R. Stoyanova, J. Solid State Electrochem. **3**, 121 (1999).

[14] I. Terasaki, Y. Sasago, and K. Uchinokura, Phys. Rev. B **56**, R12685 (1997).

[15] J. B. Goodenough, J. Phys. Chem. Solids **6**, 287 (1958).

[16] M. Medarde, C. Dallera, M. Grioni, J. Voigt, A. Podlesnyak, E. Pomjakushina, K. Conder, Th. Neisius, O. Tjenberg, and S. N. Barilo, Phys. Rev. B **73**, 054424 (2006).

[17] G. Vanko, J. P. Rueff, A. Mattila, Z. Nemeth, and A. Shukla, Phys. Rev. B **73**, 024424 (2006).

[18] K. Knizek, Z. Jirak, J. Hejtmanek, and P. Novak, J. Phys.: Condens. Matter **18**, 3285 (2006).

[19] T. Saitoh, T. Mizokawa, A. Fujimori, M. Abbate, Y. Takeda, and M. Takano, Phys. Rev. B **55**, 4257 (1997).

[20] W.-S. Yoon, K.-B. Kim, M.-G. Kim, M.-K. Lee, H.-J. Shin, J.-M. Lee, J.-S. Lee, and C.-H. Yo, J. Phys. Chem. B **106**, 2526 (2002).

[21] M. W. Haverkort, Z. Hu, J. C. Cezar, T. Burnus, H. Hartmann, M. Reuther, C. Zobel, T. Lorenz, A. Tanaka, N. B. Brookes, H. H. Hsieh, H. J. Lin, C. T. Chen, and L. H. Tjeng, Phys. Rev. Lett. **97**, 176405 (2006).

[22] M. Abbate, J. C. Fuggle, A. Fujimori, L. H. Tjeng, C. T. Chen, R. Potze, G. A. Sawatzky, H. Eisaki, and S. Uchida, Phys. Rev. B **47**, 16124 (1993).

[23] L. A. Montoro, M. Abbate, and J. M. Rosolen, Electrochem. Solid-State Lett. **309**, 14 (1999).

[24] Z. Hu, H. Wu, M. W. Haverkort, H. H. Hsieh, H.-J. Lin, T. Lorenz, J. Baier, A. Reichl, I. Bonn, C. Felser, A. Tanaka, C. T. Chen, and L. H. Tjeng, Phys. Rev. Lett. **92**, 207402 (2004).

[25] H. M. Evjen, Phys. Rev. **39**, 675 (1932).

[26] S. Watanabe and H. Kamimura, Mater. Sci. Eng., B **3**, 313 (1989).

[27] A. Rosén, D. E. Ellis, H. Adachi, and F. W. Averill, J. Chem. Phys. **65**, 3629 (1976).

[28] P. G. Radaelli and S.-W. Cheong, Phys. Rev. B **66**, 094408 (2002).

[29] J. Akimoto, Y. Gotoh, and Y. Oosawa, J. Solid State Chem. **141**, 298 (1998).